Article

Expanding the I-II-V Phase Space: Soft Synthesis of Polytypic Ternary and Binary Zinc Antimonides

Miles A White, Katelyn J Baumler, Yunhua Chen, Amrit Venkatesh, Alan M Medina-Gonzalez, Aaron J Rossini, Julia V. Zaikina, Emory M. Chan, and Javier Vela

Chem. Mater., **Just Accepted Manuscript** • DOI: 10.1021/acs.chemmater.8b02910 • Publication Date (Web): 13 Aug 2018

Expanding the I-II-V Phase Space: Soft Synthesis of Polytypic Ternary and Binary Zinc Antimonides

Miles A. White,[1] Katelyn J. Baumler,[1] Yunhua Chen,[1,2] Amrit Venkatesh,[1,2] Alan M. Medina-Gonzalez,[1] Aaron J. Rossini,[1,2] Julia V. Zaikina,[1] Emory M. Chan,[3] and Javier Vela*[,1,2]

[1]Iowa State University, Department of Chemistry, Ames, Iowa 50011, [2]Ames Laboratory, Ames, Iowa 50011, and [3]Molecular Foundry, Lawrence Berkeley National Laboratory, Berkeley, CA 94720

ABSTRACT: Soft chemistry methods offer the possibility of synthesizing metastable and kinetic products that are unobtainable through thermodynamically-controlled, high-temperature reactions. A recent solution-phase exploration of Li-Zn-Sb phase space revealed a previously unknown cubic half-Heusler MgAgAs-type LiZnSb polytype. Interestingly, this new cubic phase was calculated to be the most thermodynamically stable, despite prior literature reporting only two other ternary phases (the hexagonal half-Heusler LiGaGe-type LiZnSb, and the full-Heusler Li_2ZnSb). This surprising discovery, coupled with the intriguing optoelectronic and transport properties of many antimony containing Zintl phases, required a thorough exploration of synthetic parameters. Here, we systematically study the effects that different precursor concentrations, injection order, nucleation and growth temperatures, and reaction time have on the solution-phase synthesis of these materials. By doing so, we identify conditions that selectively yield several unique ternary (c-LiZnSb *vs.* h*-LiZnSb), binary (ZnSb *vs.* Zn_8Sb_7), and metallic (Zn, Sb) products. Further, we find one of the ternary phases adopts a variant of the previously observed hexagonal LiZnSb structure. Our results demonstrate the utility of low temperature solution phase—soft synthesis—methods in accessing and mining a rich phase space. We anticipate that this work will motivate further exploration of multinary I-II-V compounds, as well as encourage similarly thorough investigations of related Zintl systems by solution phase methods.

INTRODUCTION

Classical Zintl phases are valence-precise compounds comprised of electropositive and electronegative elements, where the former donate their electrons to the latter to satisfy the octet rule, forming covalent bonds and adopting lone pairs of electrons.[1-3] Typical electropositive elements are either alkali/alkali earth or rare-earth metals, while electronegative elements are nonmetals, metalloids, or late transition metals.[4] Zintl compounds typically display a covalent anionic sublattice that is permeated by electropositive cations, resulting in complex crystal structures.[5] For instance, in 8 electron I-II-V half-Heusler phases, the I element donates its valence electron to stabilize a covalent zinc-blende $(II\text{-}V)^-$ network (Figure 1).[6,7] As would be expected due to their similar 8 electron network, a similar stabilization occurs in hexagonal LiGaGe-type structures, where the I^+ charge balances the wurtzite $(II\text{-}V)^-$ sublattice.[8]

Zintl compounds enable precise tuning of transport properties by manipulating stoichiometry.[9-11] Their strong correlation between structural and electronic properties has garnered substantial interest for thermoelectric applications.[12-14] Zintl phases containing Sb and Zn are of particular interest due to their structural diversity and stoichiometric tolerance. For instance, compounds belonging to the AZn_2Sb_2 (A = Ca, Sr, Ba, Eu, Yb) family are stable to both vacancies and substitutions on each crystallographic site.[15,16] In addition, these materials contain elements that are more biocompatible or more readily available than other state-of-the-art materials containing heavily regulated (Pb) or less abundant (Te) elements.[17] However, with many possible compositions and structures, it is often challenging to predictably synthesize a target compound in a phase pure manner.

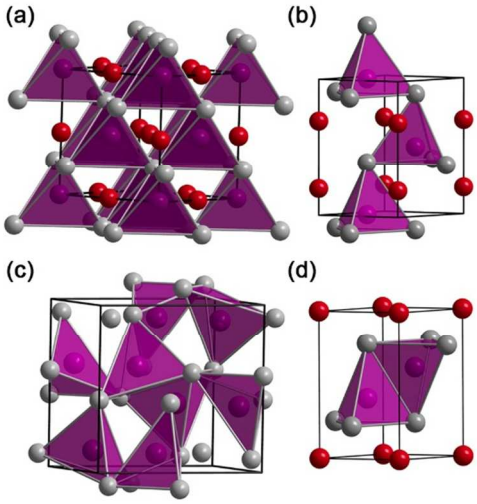

Figure 1. Unit cells and Zn polyhedra highlighting the tetrahedral coordination environments in cubic MgAgAs-type c-LiZnSb (zinc blende, a), hexagonal LiGaGe-type h-LiZnSb (wurtzite, b), binary ZnSb (c), and $CaZn_2Sb_2$-type h*-LiZnSb (extended hexagonal, d). Sb is shown in grey, Zn in purple, and Li in red.

A majority of crystalline phases are synthesized under thermodynamic control through high-temperature solid-state reactions. In contrast, a vast phase space of metastable compounds is accessible through soft chemistry techniques.[18-21] In particular, low-temperature solution-phase reactions under kinetic control enable the synthesis and isolation of new and metastable phases.[22] For example, soft synthesis enabled control over zinc-blende/wurtzite polytypism in binary II-VI and III-V semiconductors.[23-28] Recently, our group successfully expanded this approach to I-II-V ternary semiconductors, where a previously unknown, cubic half-Heusler polytype of LiZnSb was synthesized for the first time.[6] Clearly, the binary and more complex ternary Zintl phases formed from Li, Zn, and Sb are a particularly interesting family of compounds to explore utilizing kinetic control due to the large number of potential crystalline products with variable crystal chemistry.

Apart from their intriguing structural diversity, interest in Zn-Sb phases has resurged since the successful synthesis and promising thermoelectric characterization of numerous binaries, including Zn_4Sb_3, ZnSb, and Zn_8Sb_7.[29-35] A computationally derived convex hull of formation enthalpies for various binary zinc antimonides predicts ZnSb to have the most negative formation enthalpy.[36] Low-temperature, soft chemistry techniques may provide a reproducible means to observe and isolate many of these compounds. Computational surveys of antimony-based Zintl phases have revealed intriguing ternary compositions such as LiZnSb, $KAlSb_4$, and KSnSb.[37-39] However, very few solution phase syntheses have been reported to date for the binary zinc antimonides.[40-43] Further, there is only one report of a ternary LiZnSb phase prepared from solution.[6] As such, the synthesis of kinetically trapped products is an exciting frontier that remains underexplored. Here, we demonstrate the exploration of this phase space and recognize critical reaction parameters for the control of phase dimensionality. In addition to the newly mentioned cubic polytype, these efforts allow us to isolate and identify a previously unreported variant of hexagonal LiZnSb, as well as at least one Zn-Sb binary.

RESULTS AND DISCUSSION

Recent exploration of the solution phase synthesis of Zintl zinc antimonides enabled the surprising discovery of cubic LiZnSb. This previously unreported phase is the first documented example of polytypism in the family of I-II-V half Heusler compounds commonly referred to as Nowotny-Juza phases.[6] The synthesis utilizes two subsequent hot injections of *n*-butyllithium and diethylzinc into a 1-octadecene solution containing triphenylstibine (Scheme 1). Interestingly, despite prior literature reports of LiZnSb crystallizing in the hexagonal wurtzite or LiGaGe-type structure (h-LiZnSb), LiZnSb prepared in this manner adopts a cubic zinc blende or MgAgAs-type structure (c-LiZnSb) (Figure 1). Unfortunately, samples initially prepared by this general method contained a significant amount of antimony by-product.[6] To be able to isolate and study the new c-LiZnSb, and to facilitate its comparison to the better known hexagonal polytype, a more thorough study of the Li-Zn-Sb phase space was warranted. Critically, the large number of possible synthetic parameters—individual precursor concentrations, nucleation (injection) temperature (T_{inj}), growth temperature (T_{grow}), and reaction time (t)—made a traditional 'one-reaction-at-a-time' approach to conditions optimization prohibitively time consuming.

Scheme 1. Soft chemistry exploration of Li-Zn-Sb phase space (see Experimental).

$$\underset{+\ \text{n-BuLi}}{Ph_3Sb + Et_2Zn} \xrightarrow[2)\ T_{grow},\ t]{1)\ T_{inj}} \underset{ZnSb + Zn_8Sb_7}{\text{h*-LiZnSb + c-LiZnSb}}$$

Parallel screening: Optimizing multivariate parameter space. To overcome the task of meticulously exploring a vast number of possible experimental conditions, and to expedite the screening of Li-Zn-Sb phase space, we leveraged the high throughput facilities available in the Molecular Foundry at Lawrence-Berkeley National Laboratory.[44-46] We specifically used the Workstation for Automated Nanomaterials Discovery and Analysis

(WANDA), capable of heating 8 reactors from 30 to 325 °C with consistent magnetic stirring. With two liquid handling robotic arms capable of doing injections and withdrawing aliquots, WANDA greatly accelerated reaction condition screening with a high level of synthetic reproducibility that far exceeded Schlenk techniques.

Selected screening results are summarized in Table 1 and Figure 2. The general reaction in Scheme 1 fails to generate any solid products when performed at or below 200 °C. Only amorphous solids are isolated after 4 h at 200 °C, as evidenced by the lack of reflections by powder X-ray diffraction (XRD). At temperatures above 230 °C, an extended hexagonal, $CaZn_2Sb_2$-type LiZnSb ternary (h*-LiZnSb, see below) is observed, which decomposes into binary ZnSb after continued heating (> 2 h). Heating at or above 300 °C quickly results in the formation of metallic (zerovalent) antimony, and continued heating fails to produce additional crystalline products.

Table 1. Selected results from parallel synthetic screening.[a]

#	[Li] (mM)	[Zn] (mM)	[Sb] (mM)	T_{Grow} (°C)	T_{Inj} (°C)	t (h)	Product(s)[b]
1	40	40	40	260	200	4	h*-LiZnSb and Sb
2	40	80	320	260	150	1	h*-LiZnSb
3	40	80	320	260	150	2	h*-LiZnSb, and ZnSb
4	40	40	320	260	150	0.5	No rxn.
5	40	40	320	260	150	1	h*-LiZnSb
6	40	40	320	260	150	4	h*-LiZnSb, c-LiZnSb, and ZnSb
7	40	40	80	240	200	2	h*-LiZnSb
8	40	40	320	300	200	4	Sb
9	80	40	320	260	150	1	Sb
10	40	40	400	300	250	4	c-LiZnSb and Sb

[a]Performed in ODE according to Scheme 1 (see Experimental).
[b]Determined by powder XRD.

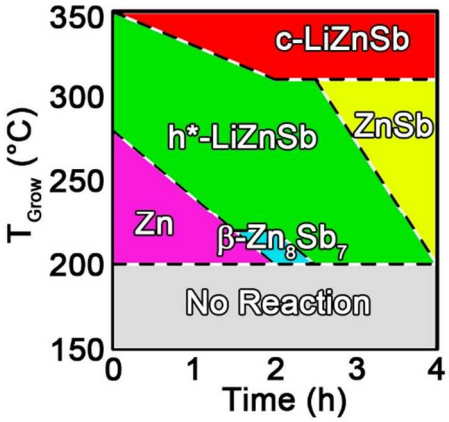

Figure 2. Li-Zn-Sb phase space diagram using optimized synthetic conditions (T_{inj} = 150 °C, [Li] = [Zn] = 40 mM, [Sb] = 160 mM, see Experimental).

We next examined the effect that changing the concentrations of Li, Zn, and Sb precursors has on the rate and final outcome of the reaction. Interestingly, Sb precursor concentration is the most important parameter in determining phase selectivity. At a fixed growth temperature of 260 °C, identical precursor concentrations of [Li] = [Zn] = [Sb] = 40 mM result in no reaction prior to 2 h, when the primary product becomes amorphous antimony. Continued heating at 260 °C results in a mixture of elemental Sb and h*-LiZnSb (Table 1, entry 1). However, increasing the Sb concentration to [Sb] = 80 mM while keeping other conditions constant results in the formation of h*-LiZnSb after 2 h, followed by its decomposition into ZnSb after 4 h. Further increasing the Sb precursor concentration to either [Sb] = 160 mM or 320 mM causes more rapid formation of h*-LiZnSb, but also faster decomposition into ZnSb binary. Using [Zn] = 80 mM, [Sb] = 320 mM, and [Li] = 40 mM at 260 °C results in h*-LiZnSb formation after 1 h, then a majority ZnSb phase after 2 h (Table 1, entries 2–3). Increasing the concentration of Li to [Li] = 80 mM causes rapid reduction of triphenylstibine and yields exclusively metallic antimony.

Along with growth temperature, reaction time, and precursor concentrations, injection parameters can have a profound effect on product formation. We find that the order of injection (addition) of precursors does not have a noticeable impact on our reaction. Additionally, the time delay between the injections of *n*-butyllithium and diethylzinc does not change the identity or relative yield of products at a concentration of [Sb] = 80 mM. However, at a higher concentration of [Sb] = 320 mM, a longer delay causes the formation of Sb metal, which is otherwise only observed at more elevated growth temperatures or higher concentrations of Li. Interestingly, even in this situation, metallic Sb becomes observable after 4 h reaction, only. We also studied the effect of injection temperature. For both T_{inj} = 150 °C and 200 °C, the same

products and relative compositions are observed. Figure 2 shows a phase space diagram constructed for [Li] = [Zn] = 40 mM, [Sb] = 160 mM, and T_{inj} = 150 °C.

Selectivity for cubic- *vs.* extended hexagonal-LiZnSb. Using [Li], [Zn], and [Sb] concentrations of 40 mM, 40 mM, and 80 mM, respectively, and growth temperatures in the 220–310 °C range, we succeeded in selectively synthesizing h*-LiZnSb (see description below). At lower growth temperatures, phase pure h*-LiZnSb forms very slowly (*e.g.*, requiring over 2 h at 220 °C) while, at higher growth temperatures, h*-LiZnSb forms very quickly (*e.g.*, < 10 min at 310 °C).

Increasing the concentration of Sb above 300 mM, we also succeeded in selectively synthesizing c-LiZnSb. As noted previously, this phase is always found to form in the presence of an elemental Sb impurity or "seed", which can arise from partial reduction of the Sb precursor. For example, although c-LiZnSb is not observed with an injection temperature of 150 °C, an injection temperature of 200 °C caused it to form at longer than 2 h reaction. In addition, phase evolution studies followed by powder XRD show h*-LiZnSb decomposes into c-LiZnSb (see below).

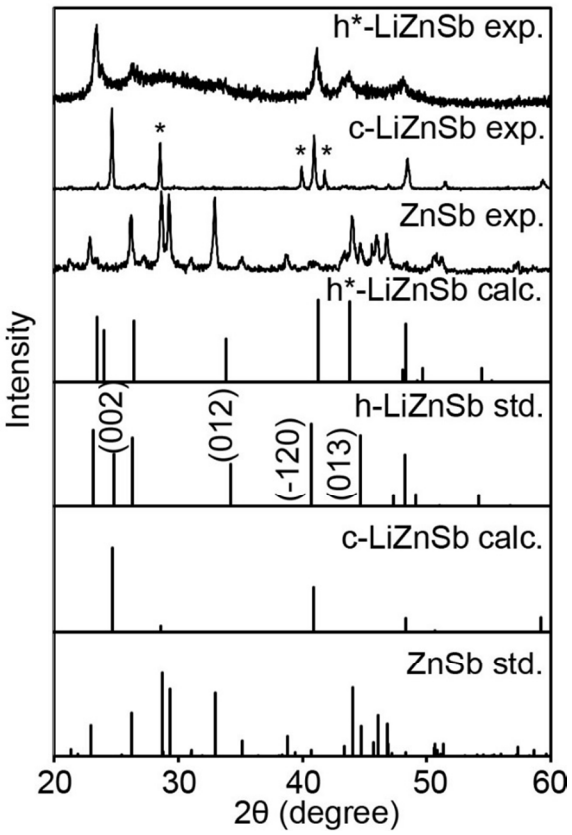

Figure 3. Powder XRD patterns of h*-LiZnSb, c-LiZnSb (* = Sb metal impurity), and binary ZnSb. Also shown are the calculated (h*-LiZnSb and c-LiZnSb) and reported (h-LiZnSb and ZnSb) standard patterns (ICSD Nos. 42064 and 43653).

Extended hexagonal LiZnSb. Despite the powder X-ray diffraction pattern of h*-LiZnSb closely resembling the known LiGaGe-type h-LiZnSb, there are some inconsistencies that indicate a deviation from this ideal structure type (Figure 3). Notably, reflections corresponding to the 002 and 012 planes are substantially suppressed. Additionally, the peak position of the -120 and 013 planes poorly agree with the standard pattern and are shifted in opposite directions (-120 to higher and 013 to lower 2θ values). These differences can be accounted for by slight changes in lattice parameters; specifically, a 1.4% suppression in *a* and *b* along with a 3.4% expansion along *c*. A literature survey of compounds that possess a similar *a*/*c* ratio reveals a large class of ternary zinc antimonides that crystallize in the $CaZn_2Sb_2$-type structure.

The $CaZn_2Sb_2$ structure is a layered variant of the LiGaGe structure type where slabs of tetrahedrally coordinated $[Zn_2Sb_2]^{2-}$ are separated by layers of Ca^{2+} (Figure 4). The structure of this Zintl phase has been thoroughly investigated as a promising thermoelectric.[47,48] There is ample precedent for all crystallographic positions having substantial mixing and disorder. In the case of a ternary phase forming from Li, Zn, and Sb, a very likely site preference would be Li^+ replacing Ca^{2+} to form the cationic layer, while Zn and Sb continue to form the tetrahedral anionic slab.

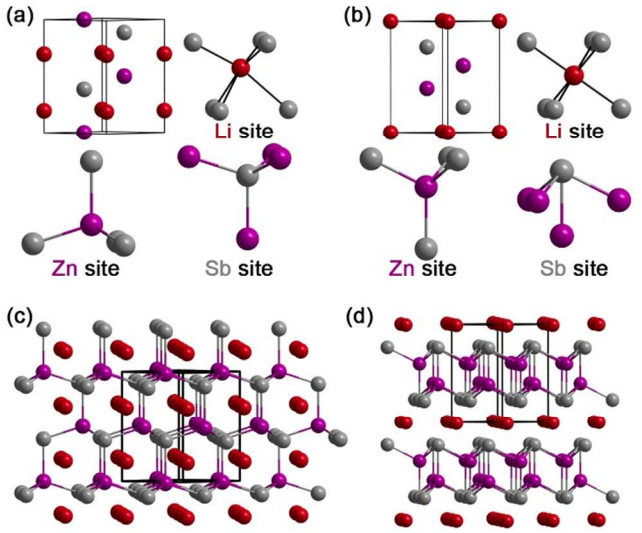

Figure 4. Unit cell and local environments for (a) h-LiZnSb and (b) h*-LiZnSb. Extended supercell of the two ternary hexagonal structures highlighting the 3D (c) and 2D (d) nature of the tetrahedral [ZnSb] anionic layer.

The $CaZn_2Sb_2$-type has three unique crystallographic sites, one for each element (Figure 4). To properly charge balance, the anionic slab needs to have an overall charge of -1 per unit cell, to be compensated by the one Li^+ per unit cell. This can either be achieved through a slightly zinc rich tetrahedral layer of $[Zn_{2.2}Sb_{1.8}]^-$, or through vacancies in the Sb position to give a composition of $[Zn_2Sb_{1.66}]^-$. Additionally, doping Zn^{2+} into Li^+ sites within the cationic layer is supported by their nearly identical effective ionic radii: 76 pm for Li^+ *vs*. 74 pm for Zn^{2+},[49] as in the case of Li_2ZnSb.[50] It is possible these three options could occur together in a relatively disordered structure.

To probe possible structures, the Vienna Ab Initio Simulation Package (VASP) was used.[51,52] A conjugated algorithm was applied to the structural optimization with an 11×11×11 Monkhorst-Pack *k*-point grid.[53] The theoretical lattice parameters of $LiZn_2Sb_2$, calculated using the LDA, are a = 4.11 Å and c = 7.20. This is slightly smaller (by only 3.0 %) than the experimentally observed lattice constants of a = 4.43 Å and c = 7.40 Å, which agrees well with the typical level of underestimation obtained with LDA for similar systems.[54] Aside from changes in lattice parameters, no further changes occurred in the local site environments or structure.

Phase evolution: From Zn unary seeds to LiZnSb ternary. To further probe the formation mechanism of a ternary phase at the microscopic level, we followed the phase evolution of h*-LiZnSb over time. More specifically, we injected triphenylstibine (80 mM) to a solution of 40 mM n-butyl lithium and 40 mM diethylzinc in a mixture of 1-octadecene and trioctylphosphine at 240 °C, retrieved small aliquots at different times, and isolated and analyzed the solids produced by XRD, X-ray photoelectron spectroscopy (XPS), and transmission electron microscopy (TEM) (see Experimental). The injection of triphenylstibine into a solution of Li and Zn precursors helps in generating the intermediate Zn metal seeds that are required for this reaction, and is different from what was utilized in our original synthesis of MgAgAs-type c-LiZnSb.

Immediately upon injection, the only crystalline phase present is Zn metal, formed from the reduction of diethylzinc by *n*-butyllithium (Figure 5).[55] The amount of Zn decreases over the next 15 min, and is no longer observable after 30 min. Also, a large amorphous peak evolves in the first 15 min that is absent at longer time steps. This peak has a maximum intensity centered around 2θ = 28.48 degrees, which corresponds to the most intense reflection of elemental Sb. XPS of early reaction (12 min) samples shows the coexistence of three peaks in the Sb $3d_{5/2}$ and $3d_{3/2}$ regions (Figure 6). The most intense peak is located at 528.3 eV and 537.8 eV for $3d_{5/2}$ and $3d_{3/2}$, respectively, in good agreement with zerovalent Sb.[56] Additional XPS peaks observed at higher binding energies are assigned to higher Sb oxidation states of +3 and +5, likely corresponding to free (unreacted) and surface-bound triphenylstibine.

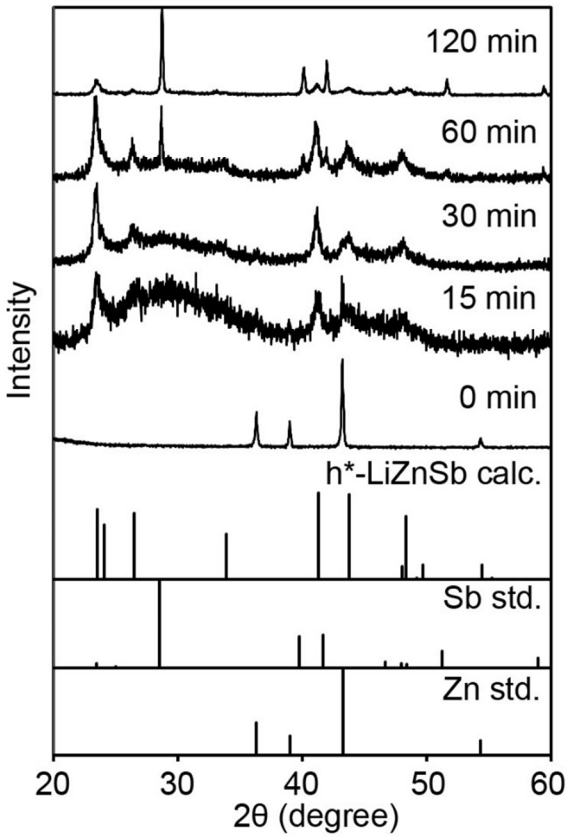

Figure 5. Powder XRD of solids isolated during the optimized synthesis of h*-LiZnSb (T_{inj} = 150 °C, T_{grow} = 280 °C, [Li] = [Zn] = 40 mM, [Sb] = 80 mM, see Experimental).

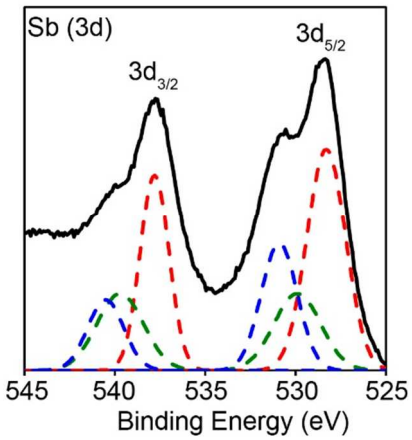

Figure 6. XPS of solids isolated during the optimized synthesis of h*-LiZnSb (T_{inj} = 150 °C, T_{grow} = 280 °C, t = 12 min, [Li] = [Zn] = 40 mM, [Sb] = 80 mM, see Experimental). Typical peak positions of Sb^{5+}, Sb^{3+}, and Sb^0 are

given by the dashed blue, green, and red curves, respectively.[53]

To investigate the spatial relationship between the initially formed Sb phase and Zn seeds, we used energy-dispersive X-ray spectroscopy (EDX) (Figure 7). Interestingly, the Zn and Sb are found colocalized across particles instead of phase segregated. Their average elemental composition is 48.3±0.7% and 51.7±0.7% for Zn and Sb, respectively, closely matching the anticipated composition of 1:1. Observed lattice fringes correspond to the most intense reflection (011) of Zn. Further, selected area electron diffraction (SAED) shows sharp and diffuse rings that correspond to Zn and Sb reflections, respectively (see SI).

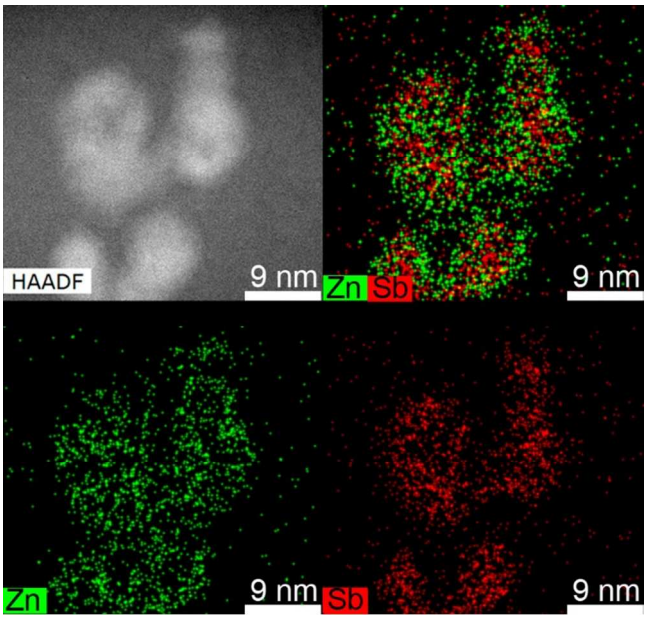

Figure 7. Representative EDX elemental mapping of h*-LiZnSb produced after 12 min at 280 °C (T_{inj} = 150 °C, T_{grow} = 280 °C, t = 12 min, [Li] = [Zn] = 40 mM, [Sb] = 80 mM, see Experimental).

These data support a ternary formation mechanism that progresses in three steps (Scheme 2). First, Zn seeds are formed by the rapid reduction of diethylzinc from *n*-butyllithium. Second, amorphous Sb surrounds the Zn seeds and, finally, interfacial solid-state diffusion occurs between these two domains, resulting in crystalline h*-LiZnSb. Unfortunately, due to the atomic number threshold of EDX, it is not possible to track the position of the light Li throughout the reaction using this technique. Li is likely either intercalated into the Zn seeds or amorphous Sb. Powder XRD data of a '0 min' sample (removed and isolated immediately upon injection) does not show a change in lattice constant, and the peaks are not substantially broadened, which makes the intercalation of Li into the Zn seeds unlikely. This mechanism is consistent with what was observed for LiZnP, as well as binary phosphides.[55,57-63]

Scheme 2. Mechanism of formation h*-LiZnSb.

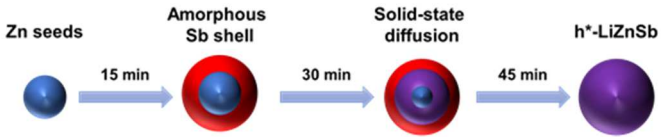

Stability of hexagonal- *vs.* cubic-LiZnSb. Previous calculations indicated that c-LiZnSb is more thermodynamically stable than its better known hexagonal polytype.[6,8] Given that solution phase synthesis allowed us to isolate an extended hexagonal (h*-LiZnSb) version of LiZnSb, we sought to determine whether this phase could transform into c-LiZnSb through thermal annealing.

In situ XRD experiments performed on the 17-BM beamline at Argonne National Laboratory's Advanced Photon Source (APS) show similar decomposition pathways for h*-LiZnSb and c-LiZnSb. As expected from the strong 3D covalent $(ZnSb)^-$ zinc-blende sublattice, the thermal stability of c-LiZnSb is higher than that of the pseudo-two-dimensional (2D) layered h*-LiZnSb (Figure 4). Decomposition temperatures are 360 °C for c-LiZnSb *vs.* 240 °C for h*-LiZnSb. Interestingly, a high thermoelectric figure of merit calculated for c-LiZnSb assumed a hot-side temperature in the range of 230–330 °C,[6] and our results indicate that this phase should be stable in this temperature range. Following ternary decomposition, metallic antimony is observed with a minority phase ZnO. Upon reaching 632 °C, Sb melts and ZnO is the only crystalline product. Critically, while the major decomposition products of h*-LiZnSb were also Sb and ZnO, a small peak that corresponds to the most intense (111) reflection of c-LiZnSb begins to evolve at 335 °C. This peak becomes more intense with further heating to 632 °C but remains the minority phase with Sb metal being the majority.

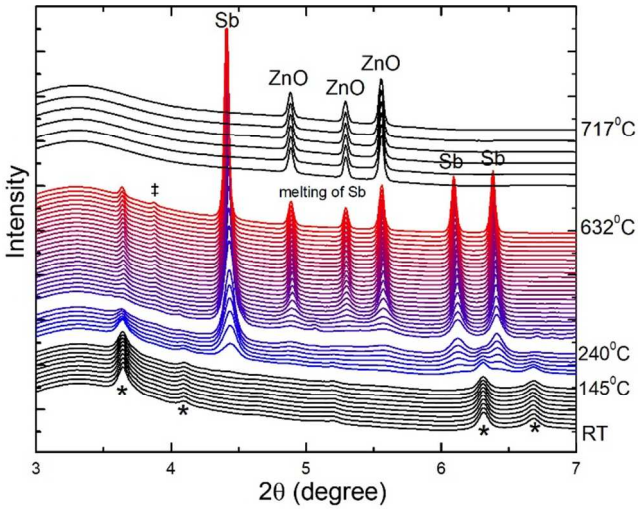

Figure 8. Variable temperature powder XRD data of h*-LiZnSb collected with a heating rate of 15 °C/min on from RT to 717 °C. Only h*-LiZnSb (labeled with *) is observed until 145 °C, where Sb begins to crystallize. h*-LiZnSb has completely decomposed by 240 °C, where Sb and ZnO are the primary crystalline components. After the melting of Sb at 632 °C, only ZnO is observed. The single peak attributed to c-LiZnSb is denoted as ‡.

In agreement with the beamline study, variable temperature or 'hot-stage' XRD and thermogravimetric/differential thermal analysis (TGA/DTA) show that heating h*-LiZnSb from room temperature (RT = 21 °C) up to 150 °C results in no significant changes. However, amorphous Sb begins to crystallize after 200 °C. This corresponds to an exothermic transition at 204 °C. Additionally, h*-LiZnSb decomposes by 250 °C. Further heating does not evolve more major phases. Elemental antimony is observed until its melting point, which coincides with a large endothermic transition at 633 °C (see SI).

Synthetic control of phase dimensionality: Ternary *vs.* binary (Li)-Zn-Sb. Exploring different reaction times and antimony concentrations allowed us to successfully synthesize binary ZnSb (Figure 3). ZnSb adopts an orthorhombic crystal structure with one unique crystallographic position for both Zn and Sb (Figure 1). The coordination around Zn is a distorted tetrahedron of Sb, whereas the Sb local environment is a square pyramid comprised of four Zn and one Sb. These local environments and composition mimic the 2D tetrahedral layers contained within the ternary h*-LiZnSb described above.

ZnSb evolves after 2 h during the synthesis of h*-LiZnSb, in agreement with the low thermal stability of the latter. When [Sb] > 160 mM initial concentrations are used, ZnSb is the majority crystalline phase, becoming the only product after 4 h reaction. Therefore, longer reaction times lead to leaching of the cationic Li layers. This leaching can be inhibited through the use of excess lithium, which is consistent with the decomposition product at higher Li concentrations being c-LiZnSb. The concentrations of Zn and Li precursors also dictate whether ZnSb or c-LiZnSb are formed. When [Zn] = [Li] = 40 mM, c-LiZnSb is observed after 4 h at 260 °C. When for [Zn] = 80 mM and [Li] = 40 mM, no c-LiZnSb is observed and instead the majority phase is ZnSb.

We also find that β-Zn_8Sb_7 forms at short reaction times and 215 °C.[30] This is exciting as all zinc antimonide binaries have shown high thermoelectric figures of merit. Studies of ZnSb have been limited by its high thermal conductivity.[64,65] However, our facile, low-temperature solution-phase synthesis could be useful as a means of mitigating this problem, as it allows for reduction in grain size or nanostructuring.[13, 66-69]

Characterization of LiZnSb using solid state NMR. Surface passivating ligands are a critical feature of phases prepared by low-temperature solution-phase synthesis. To probe the presence and identity of surface-bound ligands, we utilized solid-state (ss) NMR spectroscopy. Magic angle spinning (MAS) ^{1}H spin echo ssNMR spectra of h*-LiZnSb and c-LiZnSb show distinct peaks which can be assigned to triphenylstibine (Ph_3Sb) and 1-octadecene (ODE) (see SI). This is further confirmed by ^{1}H-^{13}C cross polarization (CP) spectra, which show the same two carbonaceous species. In order to get a better understanding of the spatial relationship between Ph_3Sb and ODE, we acquired ^{1}H double quantum-single quantum (DQ-SQ) 2D spectra (Figure 9 and SI). The presence of a peak in the DQ-SQ spectrum indicates that two ^{1}H nuclei are near each other. The chemical shift in the indirect DQ dimension (δ_{DQ}) is determined by the sum of the two SQ chemical shifts (δ_{SQ}) that generate the DQ coherence. Therefore, the signals along the diagonal are due to aggregation of similar species, while off-diagonal intensities indicate that some Ph_3Sb and ODE are close one another. For example, the ODE peak at *ca.* δ_{SQ} = 0.9 ppm and the Ph_3Sb peak at *ca.* δ_{SQ} = 7.3 ppm show a cross-peak at *ca.* δ_{DQ} = 8.2 ppm (see red line in Figure 9), indicating the close spatial proximity of some of these species on the surface.

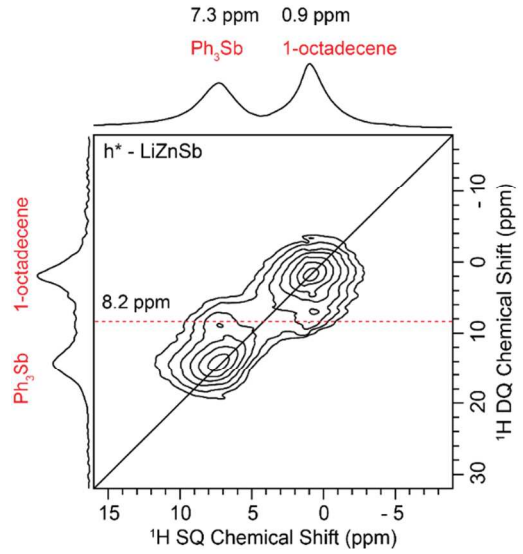

Figure 9. 2D dipolar double quantum–single quantum (DQ-SQ) correlation spectrum of h*-LiZnSb obtained using BABA dipolar recoupling.

Proton detected dipolar-refocused insensitive nuclei enhanced by polarization transfer (D-RINEPT) ssNMR experiments are selective for half-integer quadrupolar nuclei that are spatially close (dipolar coupled) to protons. Because protons are unlikely to be located within the interior (bulk) of h*-LiZnSb, 2D ^{7}Li→^{1}H D-RINEPT spectra are surface-selective, showing ^{7}Li sites that are proximal to ^{1}H on both Ph_3Sb and ODE (Figure 10). A comparison between the positive projections of the 2D D-RINEPT HETCOR spectra along the ^{7}Li dimension and ^{7}Li spin echo spectra shows relatively similar line shapes and linewidths. However, surface ^{7}Li nuclei show longer longitudinal relaxation times compared to bulk ^{7}Li (Figure 11). This may be attributed to the presence of a highly passivated surface with perfectly coordinated ligands, while the inside of the particles may contain defects, leading to a slightly shorter T_1 (see below).

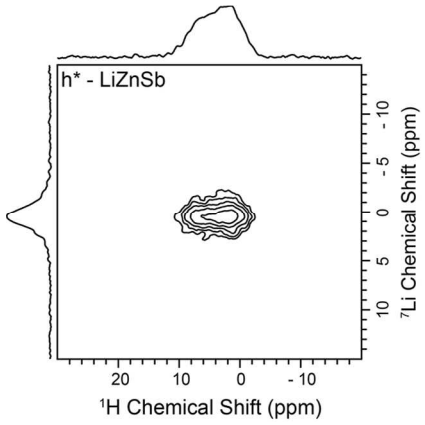

Figure 10. Surface-selective ^{1}H detected 2D ^{7}Li→^{1}H D-RINEPT of h*-LiZnSb. The appearance of through space cross-correlation peaks between Li and H indicates the surface environment of LiZnSb.

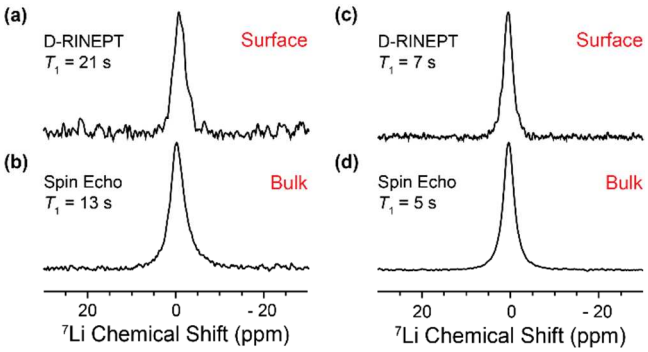

Figure 11. Comparison of the ^{7}Li spin echo spectra and positive projections of the ^{7}Li dimension from the 2D ^{7}Li→^{1}H D-RINEPT spectra for cubic MgAgAs-type LiZnSb (a, b) and h*-LiZnSb (c, d). ^{7}Li spin echo spectra show all Li chemical environments. ^{7}Li-^{1}H D-RINEPT involve magnetization transfer between ^{7}Li and ^{1}H, which only involves surface lithium sites.

Finally, we sought to use ssNMR to probe the local coordination environment around Sb. Antimony has two NMR active isotopes: ^{121}Sb and ^{123}Sb. Based on its higher natural abundance (57.2%) and smaller nuclear quadrupole moment (-54.3±1.1 fm^2), the former is more amenable to ssNMR. For example, the ^{121}Sb ssNMR spectrum of $KSb(OH)_6$ at 21.14 T using the WURST-QCPMG and quadrupolar echo pulse sequences showed an overall central transition linewidth of *ca.* 450 kHz.[2] However, even compounds with high, near-tetrahedral or octahedral symmetry can show broad ^{121}Sb ssNMR spectra. In fact, electric field gradient (EFG) parameters of various antimony-based compounds calculated using CASTEP[70] predict very large ^{121}Sb quadrupole coupling constants (C_Q). A large C_Q results in very broad ^{121}Sb ssNMR spectra, often hampering both acquisition and interpretation. The calculated C_Q of cubic LiZnSb is zero, as expected for a perfect, spherically symmetric charge distribution in a cubic space group. However, the static ^{121}Sb ssNMR spectrum of cubic LiZnSb at 9.4 T shows a single site with an unexpectedly large C_Q of 74 MHz. The substantial difference between the calculated and experimental C_Q values implies that there must be homogenously distributed impurities or defects, likely arising from multiple coloring patterns or superstructures, that must be present and result in a sizable electric field gradient and C_Q for ^{121}Sb.[6,71]

CONCLUSION

In summary, we have explored the diverse phase space generated from the solution-phase reaction between triphenylstibine, *n*-butyllithium, and diethylzinc. Depending on reaction time and temperature, we are able to selectively synthesize six different crystalline phases: Zn, Sb, ZnSb, Zn_8Sb_7, extended h*-LiZnSb, and c-LiZnSb. A previously unreported $CaZn_2Sb_2$-type ternary, extended hexagonal LiZnSb is a layered variant of the hexagonal LiGaGe-type LiZnSb seen from high temperature reactions. Antimony concentration and temperature are the main factors affecting the selectivity between hexagonal $CaZn_2Sb_2$-type and cubic MgAgAs-type LiZnSb (the latter is formed at higher Sb concentrations and higher growth temperatures). Using a combination of powder XRD, XPS, and EDX, we studied the phase evolution of $CaZn_2Sb_2$-type LiZnSb, and identified a mechanism for its formation. Using high temperature diffraction experiments, we find that cubic MgAgAs-type LiZnSb is more thermodynamically stable than $CaZn_2Sb_2$-type LiZnSb. Further, the latter appears to transition to MgAgAs-type c-LiZnSb upon heating.

A staple of crystalline semiconductors prepared by low-temperature solution-phase or soft chemistry methods is the presence of surface passivating ligands. Using solid state (ss) NMR, we have identified the presence of ODE and Ph_3Sb on the surface of both cubic MgAgAs-type and $CaZn_2Sb_2$-type LiZnSb crystallites. Additionally, ssNMR confirms the presence of Li within these crystals. Finally, ssNMR supports multiple coloring patterns or superstructures are present in the cubic MgAgAs-type structure. In conclusion, the Li-Zn-Sb phase space appears to be extremely rich with many promising thermoelectric materials already revealed. We hope that this report will spark additional investigation into the solution phase synthesis and optimization of binary and ternary zinc antimonides.

EXPERIMENTAL

Materials. 1-octadecene (ODE, technical grade, 90%), diethylzinc (Et_2Zn, 56 wt. % Zn), and *n*-butyllithium (*n*-BuLi, 1.6 M in hexane) were purchased from Sigma; triphenylstibine (Ph_3Sb, 97%) and tri-*n*-octylphosphine (TOP, 97%) were purchased from Strem. All chemicals were used as received. Stock solutions were made with ODE as the solvent with concentrations of 0.8 M, 0.4 M, and 0.4 M for Ph_3Sb, *n*-BuLi, and Et_2Zn, respectively.

Synthesis. Note: In all cases, ODE and/or TOP were degassed under dynamic vacuum prior reaction (0.5–2 h at 120 °C). *Parallel Screening.* 0.4 M Ph_3Sb (1–8 mL, 40–320 mM) in ODE was diluted to a total volume of 8 mL (with ODE and/or TOP), and heated to the desired T_{inj}. 0.4 M Et_2Zn (1–2 mL, 40–80 mM) in ODE and 0.4 M *n*-BuLi (1–2 mL, 40–80 mM) were injected in quick succession. The mixture was heated and kept at the desired T_{grow}. *Optimized Synthesis of h*-LiZnSb ternary.* TOP (3 mL) and ODE (4 mL) were heated to 120 °C under Ar. A mixture of 0.4 M *n*-BuLi (1 mL, 40 mmol) and 0.4 M Et_2Zn (1 mL, 40 mmol) in ODE was injected. The mixture was heated and kept at 240 °C for 15 min. Next, 0.8 M Ph_3Sb (1 mL, 80 mmol) was injected, and the mixture heated and kept at 280 °C for 30 min. *Optimized Synthesis of c-LiZnSb ternary*. A mixture of 0.4 M *n*-BuLi (1 mL, 40 mmol) and 0.4 M Et_2Zn (1 mL, 40 mmol) in ODE was injected into a solution containing TOP (3 mL) and ODE (4 mL) at 120 °C. The mixture was heated and kept at 240 °C for 15 min, followed by heating to 310 °C. 0.8 M Ph_3Sb (0.5 mL, 40 mmol) in ODE was injected and the temperature maintained at 310 °C for 2 h. *Optimized Synthesis of ZnSb binary.* 0.8 M Ph_3Sb solution in ODE (5 mL, 400 mmol) and TOP (3 mL) were heated to 185 °C. A mixture of 0.4 M Et_2Zn (1 mL, 40 mmol) and 0.4 M *n*-BuLi (1 mL, 40 mmol) in ODE was injected. This mixture was then heated and kept at 220 °C for 4 h. *Isolation.* After cooling to RT, solids were isolated after twice diluting with toluene (3–10 mL), crashing with ethanol (5 mL), and centrifugation (5000 rpm for 10 min).

Characterization. Powder X-ray diffraction (PXRD) data were measured using Cu Kα radiation on a Rigaku Ultima IV diffractometer. Transmission electron microscopy (TEM) and energy dispersive X-ray spectroscopy (EDX) were conducted on carbon-coated copper grids using a FEI Titan Themis Cubed Aberration Corrected Scanning Transmission Electron Microscope.

XPS. X-Ray photoemission spectroscopy (XPS) measurements were performed using a Kratos Amicus/ESCA 3400 instrument. The sample was irradiated with 240 W non-monochromated Mg Kα x-rays, and photoelectrons emitted at 0° from the surface normal were energy analyzed using a DuPont type analyzer. The pass energy was set at 75 eV. CasaXPS was used to process raw data files.

Hot-Stage XRD. Variable temperature powder XRD was conducted using a Panalytical X'Pert Pro MPD system fitted with an Anton Paar HTK1200N furnace and an X'Celerator detector. Diffraction measurements with Cu-K$_\alpha$ radiation were taken at temperature steps from 25°C to 550 °C. The sample was heated to the specified temperature and held during the measurement under flowing helium.

Variable temperature synchrotron powder XRD data were collected at the synchrotron beamline: 17-BM at the Advanced Photon Source (APS) at Argonne National Lab (ANL). Samples were loaded into silica capillaries (0.5 mm ID; 0.7 mm OD) and sealed under vacuum. The sealed capillaries were placed inside a secondary shield capillary in the flow furnace, with a thermocouple set as

close as possible to the end of the inner capillary.[72] Data were collected with λ = 0.24128 Å on heating from RT to ~700 °C and on cooling; with the heating rate of 10–15 °C/min, and 20 °C /min for cooling. Diffraction data were acquired continuously with 1 min collection times. Temperature calibration was applied by calibration using the melting points of elemental Sn, Sb, Ge.

TGA-DTA. Thermal analysis was conducted using a TA Instruments SDT 2960 (simultaneous DTA-TGA). The apparatus has a micro-balance sensitivity of 0.1 micro-grams and temperature sensitivity (for DTA) of 0.001 °C. The apparatus can be used to study material transformations over a temperature range from ambient to 1500 °C. Experiments were conducted in an N_2 atmosphere (dynamic, flow rate = 100 mL/min), from ambient to 690 °C at a scanning rate of 5 °C/min. The experiments were conducted with alumina sample pans (size = 90 μL). Calcined alumina was used in the reference pan. A nominal sample size of 20 mg was used.

Solid-state NMR. All moderate-field [B_0 = 9.4 T, $\nu_0(^1H)$ = 400.5 MHz, $\nu_0(^7Li)$ = 155.6 MHz, $\nu_0(^{13}C)$ = 100.7 MHz, $\nu_0(^{121}Sb)$ = 95.8 MHz] solid-state (ss) NMR experiments were performed on a Bruker Avance III HD spectrometer with a wide-bore magnet. A Bruker 1.3 mm HX double resonance MAS probe was used to perform all fast-MAS experiments at a spinning rate (ν_{rot}) of 45 kHz. ^1H NMR shifts were referenced to neat Tetramethylsilane using adamantane ($\delta_{iso}(^1H)$ = 1.82 ppm) as a secondary standard. Previously published relative NMR frequencies[73] were used to indirectly reference ^7Li, ^{13}C and ^{121}Sb chemical shifts. All experiments were performed using optimum recycle delays of 1.3 × T_1; the recycle delays and number of scans of all experiments are listed in the SI. All the NMR spectra were processed in Topspin 4.0.

^1H ssNMR. ^1H MAS NMR spectra were acquired using a Hahn echo sequence; all NMR experiments were performed with 2.5 μs and 5 μs π/2 and π pulses respectively on the ^1H channel. ^1H radiofrequency (RF) fields were calibrated directly on each sample using a π/2-spin-lock pulse sequence to find the 2nd order rotary resonance recoupling (R^3) conditions (2 × ν_{rot}).[74] ^1H DQ-SQ 2D spectra were acquired using the BABA recoupling method [75]with a one rotor cycle duration each for DQ excitation and reconversion, and π/2 pulse lengths of 2.5 μs.

^7Li ssNMR. ^7Li MAS NMR spectra were acquired using a Hahn-echo sequence with central transition (CT) selective π/2 and π pulses lengths of 1.5 μs and 3 μs respectively. ^1H detected ^7Li–^1H D-RINEPT spectra were obtained with a short recoupling time of 6 rotor cycles per recoupling block for near-surface characterization. The T_1 of the surface ^7Li sites were obtained using the ^1H detected ^7Li–^1H D-RINEPT pulse sequence with an additional saturation recovery block before the D-RINEPT transfer block.[76]

^{13}C ssNMR. ^1H detected $^1H\{^{13}C\}$ CP-HETCOR and direct detected ^1H–^{13}C CP spectra were acquired using spin-lock RF fields of *ca.* 125 kHz and 80 kHz on the ^1H and ^{13}C channels respectively, and a ^{13}C π/2 pulse length of 2.5 μs. The ^1H spin-lock RF fields were optimized directly on the samples with a fixed ^{13}C spin-lock RF field to meet the Hartmann-Hahn CP match conditions. 80%-100% amplitude ramped spin-lock pulses were employed for the ^1H spin-lock during all CP experiments. Heteronuclear ^1H decoupling was applied at a RF field of 22.5 kHz (0.5 × ν_{rot}) for the ^7Li and ^{13}C experiments.

^{121}Sb ssNMR. The ^{121}Sb static NMR spectrum was acquired using the QCPMG pulse sequence by the piecewise frequency-stepped acquisition technique with a step-size of 250 kHz, spanning a total spectral width of *ca.* 14 MHz.[77] Each QCPMG spectrum was acquired with a spectral window of 2 MHz and an echo train comprising of 20 echoes of 20 ·s duration each. The simulated ^{121}Sb spectrum was generated using QUEST[78] with the EFG parameters showed in the SI. The CASTEP[68] program was used to calculate ^{121}Sb electric field gradient (EFG) tensor parameters of a list of antimony-based compounds according to the previous reported calculation procedure, using the Materials Studio 2017 R2 environment (see SI).[79] All calculations used the Perdew-Burke-Ernzerhof (PBE)[80] generalized gradient approximation functional with the Tkatchenko-Scheffler dispersion correction[81] and ultra-soft pseudopotentials generated *on-the-fly*. All atomic positions were optimized and P_1 symmetry was imposed on the unit cell prior to performing the NMR calculations. The NMR calculations were performed using the GIPAW method implemented in CASTEP.[82,83]

Calculations. All VASP calculations used projected augmented-wave (PAW) pseudopotentials with a cutoff energy of 500 eV and a convergence energy of $1x10^{-6}$ eV.[84] A conjugated algorithm was applied to the structural optimization with an 11 × 11 × 11 Monkhorst-pack k-points grid.[50] During structural optimizations, atomic coordinates as well as cell volumes were allowed to relax. Total energies were calculated using the tetrahedron method with Blöchl corrections applied.[85] VASP calculations treated exchange and correlation by either the local density approximation (LDA) or the Perdew-Burke-Ernzerhof (PBE) generalized gradient functional in the case of total energy calculations. Denser k-meshes were used but found to yield similar results.

ASSOCIATED CONTENT

Supporting Information. Additional XRD, NMR, TEM, EDX, TGA-DTA, and selected optoelectronic and transport

data can be found in the Supporting Information. This material is available free of charge via the Internet at http://pubs.acs.org.

AUTHOR INFORMATION

Corresponding Author

* vela@iastate.edu

Notes

The authors declare no competing financial interest.

ACKNOWLEDGMENT

J.V. thanks the U.S. National Science Foundation for a CAREER grant from the Division of Chemistry, Macromolecular, Supramolecular, and Nanochemistry Program (1253058). Y.C., A.V. and A.J.R. were supported by the U.S. Department of Energy (DOE), Office of Science, Basic Energy Sciences, Materials Science and Engineering Division. The authors thank the Molecular Foundry at Lawrence-Berkeley National Laboratory for access to the robotic synthesis user facility (4398). Work at the Ames Laboratory, the Molecular Foundry, and Advanced Photon Source at Argonne National Laboratory was supported by the Office of Science, Office of Basic Energy Sciences, of the U.S. Department of Energy under Contract Nos. DE-AC02-07CH11358, DE-AC02-05CH11231, and DE-AC02-06CH11357, respectively. The authors thank Gordie Miller for insightful discussions.

REFERENCES

(1) Toberer, E. S.; Cox, C. A.; Brown, S. R.; Ikeda, T.; May, A. F.; Kauzlarich, S. M.; Snyder, G. J. Traversing the Metal-Insulator Transition in a Zintl Phase: Rational Enhancement of Thermoelectric Efficiency in $Yb_{14}Mn_{1-x}Al_xSb_{11}$. *Adv. Funct. Mater.* **2008**, *18*, 2795–2800.

(2) Mudring, A.-V.; Corbett, J. D. Unusual Electronic and Bonding Properties of the Zintl Phase Ca_5Ge_3 and Related Compounds. A Theoretical Analysis. *J. Am. Chem. Soc.* **2004**, *126*, 5277–5281.

(3) Kim, S.-J.; Hoffman, S. D.; Fassler, T. F. $Na_{29}Zn_{24}Sn_{32}$: A Zintl Phase Containing a Novel Type of $\{Sn_{14}\}$ Enneahedra and Heteroatomic $\{Zn_8Sn_4\}$ Icosahedra. *Angew. Chem. Int. Ed.* **2007**, *46*, 3144–3148.

(4) Nesper, R. Structure and Chemical Bonding in Zintl-Phases Containing Lithium. *Prog. Solid. State Chem.* **1990**, *20*, 1–45.

(5) Zevalkink, A.; Zeier, W. G.; Pomrehn, G.; Schechtel, E.; Tremel, W.; Snyder, G. J. Thermoelectric Properties of Sr_3GaSb_3 – A Chain-Forming Zintl Compound. *Energy Environ. Sci.* **2012**, *5*, 9121–9128.

(6) White, M. A.; Miller, G. J.; Vela, J. Polytypism and Unique Site Preference in LiZnSb: A Superior Thermoelectric Reveals Its True Colors. *J. Am. Chem. Soc.* **2016**, *138*, 14574–14577.

(7) Zeier, W. G; Schmitt, J.; Hautier, G.; Aydemir, U.; Gibbs, Z. M.; Felser, C.; Snyder, G. J. Engineering Half-Heusler Thermoelectric Materials Using Zintl Chemistry. *Nat. Rev. Mater.* **2016**, *1*, 16032.

(8) White, M. A.; Medina-Gonzalez, A. M.; Vela, J. Soft Chemistry, Coloring and Polytypism in Filled Tetrahedral Semiconductors: Toward Enhanced Thermoelectric and Battery Materials. *Chem. Eur. J* **2017**, *24*, 3650–3658.

(9) Gascoin, F.; Ottensmann, S.; Stark, D.; Haile, S. M.; Snyder, G. J. Zintl Phases as Thermoelectric Materials: Tuned Transport Properties of the Compounds $Ca_xYb_{1-x}Zn_2Sb_2$. *Adv. Funct. Mater.* **2005**, *15*, 1860–1864.

(10) *Chemistry, Structure, and Bonding of Zintl Phases and Ions*; Kauzlarich, S. M., Ed.; VCH Publishers Inc., New York, 1996.

(11) *Zintl Phases: Principles and Recent Developments*, Book Series: *Structure and Bonding*; Fässler, T. F., Ed.; Volume 139, Springer, Heidelberg, 2011.

(12) Toberer, E. S.; May, A. F.; Snyder, G. J. Zintl Chemistry for Designing High Efficiency Thermoelectric Materials. *Chem. Mater.* **2010**, *22*, 624–634.

(13) Biswas, K.; He, J.; Blum, I. D.; Wu, C.-I.; Hogan, T. P.; Seidman, D. N.; Dravid, V. P.; Kanatzidis, M. G. High-Performance Bulk Thermoelectrics with All-Scale Hierarchical Architectures. *Nature* **2012**, *489*, 414–418.

(14) Brown, S. R.; Kauzlarich, S. M.; Gascoin, F.; Snyder, G. J. $Yb_{14}MnSb_{11}$: New High Efficiency Thermoelectric Material for Power Generation. *Chem. Mater.* **2006**, *18*, 1873–1877.

(15) Zevalkink, A.; Zeier, W. G.; Cheng, E.; Snyder, J.; Fleurial, J.-P.; Bux, S. Nonstoichiometry in the Zintl Phase $Yb_{1-\delta}Zn_2Sb_2$ as a Route to Thermoelectric Optimization. *Chem. Mater.* **2014**, *26*, 5710–5717.

(16) Wang, X.-J. Thermoelectric Properties and Electronic Structure of Zintl Compound $BaZn_2Sb_2$. *Appl. Phys. Lett.* **2007**, *90*, 232107.

(17) Bjerg, L.; Madsen, G. K. H.; Iversen, B. B. Enhanced Thermoelectric Properties in Zinc Antimonides. *Chem. Mater.* **2011**, *23*, 3907–3914.

(18) Men, L.; White, M. A.; Andaraarachchi, H.; Rosales, B. A.; Vela, J. Synthetic Development of Low Dimensional Materials. *Chem. Mater.* **2017**, *29*, 168–175.

(19) Uppuluri, R.; Gupta, A. S.; Rosas, A. S.; Mallouk, T. E. Soft Chemistry of Ion-Exchangeable Layered Metal Oxides. *Chem. Soc. Rev.* **2018**, *47*, 2401–2430.

(20) Seisenbaeva, G. A.; Kessler, V. G. Precursor Directed Synthesis – "Molecular" Mechanisms in the Soft Chemistry Approaches and Their Use for Template-Free Synthesis of Metal, Metal Oxide, and Metal Chalcogenide Nanoparticles and Nanostructures. *Nanoscale* **2014**, *6*, 6229–6244.

(21) Schaak, R. E.; Mallouk, T. E. Perovskites by Design: A Toolbox of Solid-State Reactions. *Chem. Mater.* **2002**, *14*, 1455–1471.

(22) Martinolich, A. J.; Kurzman, J. A.; Neilson, J. R. Polymorph Selectivity of Superconducting $CuSe_2$ Through Kinetic Control of Solid-State Metathesis. *J. Am. Chem. Soc.* **2015**, *137*, 3827–3833.

(23) Assali, S.; Gagliano, L.; Oliveira, D. S.; Verheijen, M. A.; Plissard, S. R; Feiner, L. F.; Bakkers, E. P. A. M. Exploring Crystal Phase Switching in GaP Nanowires. *Nano Lett.* **2015**, *15*, 8062–8069.

(24) Mahler, B.; Lequeux, N.; Dubertret, B. Ligand-Controlled Polytypism of Thick-Shell CdSe/CdS Nanocrystals. *J. Am. Chem. Soc.* **2010**, *132*, 953–959.
(25) Nan, W.; Niu, Y.; Qin, H.; Cui, F.; Yang, Y.; Lai, R.; Lin, W.; Peng, X. Crystal Structure Control of Zinc-Blende CdSe/CdS Core/Shell Nanocrystals: Synthesis and Structure-Dependent Optical Properties. *J. Am. Chem. Soc.* **2012**, *134*, 19685–19693.
(26) Johansson, J.; Dick, K. A.; Caroff, P.; Messing, M. E.; Bolinsson, J.; Deppert, D.; Samuelson, L. Diameter Dependence of the Wurtzite-Zinc Blende Transition in InAs Nanowires. *J. Phys. Chem. C.* **2010**, *114*, 3837–3842.
(27) Joyce, H. J.; Wong-Leung, J.; Gao, Q.; Tan, H. H.; Jagadish, C. Phase Perfection in Zinc Blende and Wurtzite III – V Nanowires Using Basic Growth Parameters. *Nano Lett.* **2010**, *10*, 908–915.
(28) Karan, N. S.; Sarkar, S.; Sarma, D. D.; Kundu, P.; Ravishankar, N.; Pradhan, N. Thermally Controlled Cyclic Insertion/Ejection of Dopant Ions and Reversible Zinc Blende/Wurtzite Phase Changes in ZnS Nanostructures. *J. Am. Chem. Soc.* **2011**, *133*, 1666–1669.
(29) Caillat, T.; Fleurial, J. P; Borshchevsky, A. Preparation and Thermoelectric Properties of Semiconducting Zn_4Sb_3. *J. Phys. Chem. Solids* **1997**, *58*, 1119–1125.
(30) Zhang, L. T.; Tsutsui, M.; Ito, K.; Yamaguchi, M. Effects of ZnSb and Zn Inclusions on the Thermoelectric Properties of β-Zn_4Sb_3. *J. Alloy Compd.* **2003**, *358*, 252–256.
(31) Pothin, R.; Ayral, R. M.; Berche, A.; Dranier, D.; Rouessac, F.; Jund, P. Preparation and Properties of ZnSb Thermoelectric Material Through Mechanical-Alloying and Spark Plasma Sintering. *Chem. Eng. J.* **2016**, *299*, 126–134.
(32) Wang, J.; Kovnir, K. Elusive β-Zn_8Sb_7: A New Zinc Antimonide Thermoelectric. *J. Am. Chem. Soc.* **2015**, *137*, 12474–12477.
(33) Lin, J.; Li, X.; Qiao, G.; Wang, Z.; Carrete, J.; Ren, Y.; Ma, L.; Fei, Y.; Yang, B.; Lei, L.; Li, J. Unexpected High-Temperature Stability of β-Zn_4Sb_3 Opens the Door to Enhanced Thermoelectric Performance. *J. Am. Chem. Soc.* **2014**, *136*, 1497–1504.
(34) Mozharivskyj, Y.; Janssen, Y.; Harringa, J. L.; Kracher, A.; Tsokol, A. O.; Miller, G. J. $Zn_{13}Sb_{10}$: A Structural and Landau Theoretical Analysis of Its Phase Transitions. *Chem. Mater.* **2006**, *18*, 822–831.
(35) Snyder, G. J.; Christensen, M.; Nishibori, E.; Caillat, T.; Iversen, B.B. Disordered Zinc in Zn_4Sb_3 with Phonon-Glass and Electron-Crystal Thermoelectric Properties. *Nat. Mater.* **2004**, *3*, 458–463.
(36) He, X.; Fu, Y.; Singh, D. J.; Zhang, L. Stability, Electronic Structures and Thermoelectric Properties of Binary Zn-Sb Materials. *J. Mater. Chem. C.* **2016**, *4*, 11305–11312.
(37) Madsen, G. K. H. Automated Search for New Thermoelectric Materials: The Case of LiZnSb. *J. Am. Chem. Soc.* **2006**, *128*, 12140–12146.
(38) Ortiz, B. R.; Gorai, P.; Krishna, L.; Mow, R.; Lopez, A.; McKinney, R.; Stevanovic, V.; Toberer, E. S. Potential for High Thermoelectric Performance in n-Type Zintl Compounds: A Case Study of Ba Doped $KAlSb_4$. *J. Mater. Chem. A* **2017**, *5*, 4036–4046.
(39) Huang, S.; Liu, H. J.; Fan, D. D.; Jiang, P. H.; Liang, J. H.; Cao, G. H.; Liang, R. Z.; Shi, J. First-Principles Study of the Thermoelectric Properties of the Zintl Compound KSnSb. *J. Phys. Chem. C* **2018**, *8*, 4217–4223.
(40) Kieslich, G.; Birkel, C. S.; Stewart, A.; Kolb, U.; Tremel, W. Solution Synthesis of Nanoparticular Binary Transition Metal Antimonides. *Inorg. Chem.* **2011**, *50*, 6938–6943.
(41) Denoix, A.; Solaiappan, A.; Ayral, R. M.; Rouessac, F.; Tedenac, J. C. Chemical Route for Formation of Intermetallic Zn_4Sb_3 Phase. *J. Solid State Chem.* **2010**, *183*, 1090–1094.
(42) Birkel, C. S.; Mugnaioli, E.; Gorelik, T.; Kolb, U. Panthofer, M.; Tremel, W. Solution Synthesis of a New Thermoelectric $Zn_{1+x}Sb$ Nanophase and Its Structure Determination Using Automated Electron Diffraction Tomography. *J. Am. Chem. Soc.* **2010**, *132*, 9881–9889.
(43) Mai, N. T.; Mott, D. M.; Higashimine, K.; Maenosono, S. One-Pot Chemical Synthesis of Zinc Antimonide Nanoparticles as Building Blocks for Nanostructured Thermoelectric Materials. *Chem. Lett.* **2012**, *41*, 1529–1531.
(44) Owen, J. S.; Chan, E. M.; Liu, H.; Alvisatos, A. P. Precursor Conversion Kinetrics and the Nucleation of Cadmium Selenide Nanocrystals. *J. Am. Chem. Soc.* **2010**, *132*, 18206–18213.
(45) Chan, E. M.; Xu, C.; Mao, A. W.; Han, G.; Owen, J. S.; Cohen, B. E.; Milliron, D. J. Reproducible, High-Throughput Synthesis of Colloidal Nanocrystals for Optimization in Multidimensional Parameter Space. *Nano Lett.* **2010**, *10*, 1874–1885.
(46) Chan, E. M.; Han, G.; Goldberg, J. D.; Gargas, D. J.; Ostrowski, A. D.; Schuck, P. J.; Cohen, B. E.; Milliron, D. J. Combinatorial Discovery of Lanthanide-Doped Nanocrystals with Spectrally Pure Upconverted Emission. *Nano Lett.* **2012**, *12*, 3839–3845.
(47) Zhu, T. J.; Yu, C.; He, J.; Zhang, S. N.; Zhao, X. B.; Tritt, T. M. Thermoelectric Properties of Zintl Compound $YbZn_2Sb_2$ with Mn Substitution in Anionic Framework. *J. Electron. Mater.* **2009**, *38*, 1068–1071.
(48) Zhang, X.; Peng, K.; Guo, L.; Yan, Y.; Zhan, H.; Lu, X.; Gu, H.; Zhou, X. Effects of Lanthanum Substitution on Thermoelectric Properties of $YbZn_2Sb_2$. *J. Electron. Mater.* **2017**, *46*, 2611–2615.
(49) Shannon, R. D. Revised Effective Ionic Radii and Systematic Studies of Interatomic Distances in Halides and Chalcogenides. *Acta Cryst.* **1976**, *32*, 751–767.
(50) Schroeder, G.; Schuster, H. -U. Röntgenographische Untersuchungen im System Lithium-Zink-Antimon. *Z. Anorg. Allg. Chem.* **1977**, *431*, 217–220.
(51) Kresse, G.; Furthmuller, J. Efficiency of Ab-Initio Total Energy Calculations for Metals and Semiconductors Using a Plane-Wave Basis Set. *J. Comput. Mater. Sci.* **1996**, *6*, 15–50.

(52) Kresse, G.; Furthmuller, J. Efficient Iterative Schemes for Ab Initio Total-Energy Calculations Using a Plane-Wave Basis Set. *Phys. Rev. B*: *Condens. Matter Mater. Phys.* **1996**, *54*, 11169–11186.
(53) Monkhorst, H. J.; Pack, J. D. Special Points for Billouin-Zone Integrations. *Phys. Rev. B* **1976**, *13*, 5188–5192.
(54) Haas, P.; Tran, F.; Blaha, P. Calculation of the Lattice Constant of Solids with Semilocal Functionals. *Phys. Rev. B* **2009**, *79*, 085104.
(55) White, M. A.; Thompson, M. J.; Miller, G. J.; Vela, J. Got LiZnP? Solution Phase Synthesis of Filled Tetrahedral Semiconductors in the Nanoregime. *Chem. Commun.* **2016**, *52*, 3497–3499.
(56) Moulder, J. F.; Stickle, W. F.; Sobol, P. E.; Bomben, K. D. *Handbook of X-ray Photoelectron Spectroscopy: A Reference Book of Standard Spectra for Identification and Interpretation of XPS Data*; Chastain, J., King, R. C. Jr., Eds.; ULVAC-PHI: Japan, 1995.
(57) Mobarok, M. H.; Luber, E. J.; Bernard, G. M.; Peng, L.; Wasylishen, R. E.; Buriak, J. M. Phase-Pure Cyrstalline Zinc Phosphide Nanoparticles: Synthetic Approaches and Characterization. *Chem. Mater.* **2014**, *26*, 1925–1935.
(58) Henkes, A. E.; Vasquez, Y.; Schaak, R. E. Converting Metals into Phosphides: A General Strategy for the Synthesis of Metal Phosphide Nanocrystals. *J. Am. Chem. Soc.* **2007**, *129*, 1896–1897.
(59) Henkes, A. E.; Schaak, R. E. Trioctylphosphine: A General Phosphorus Source for the Low-Temperature Conversion of Metals into Metal Phosphides. *Chem. Mater.* **2007**, *19*, 4234–4242.
(60) Carenco, S.; Portehault, D.; Boissiere, C.; Mezailles, N.; Sanchez, C. Nanoscaled Metal Borides and Phosphides: Recent Developments and Perspectives. *Chem. Rev.* **2013**, *113*, 7981–8065.
(61) Chiang, R.-K.; Chiang, R.-T. Formation of Hollow Ni_2P Nanoparticles Based on the Nanoscale Kirkendall Effect. *Inorg. Chem.* **2007**, *46*, 369–371.
(62) Muthuswamy, E.; Kharel, P. R.; Lawes, G.; Brock, S. L. Control of Phase in Phosphide Nanoparticles Produced by Metal Nanoparticle Transformation: Fe_2P and FeP. *ACS Nano* **2009**, *3*, 2383–2393.
(63) Brock, S. L.; Senevirathne, K. Recent Developments in Synthetic Approaches to Transition Metal Phosphide Nanoparticles for Magnetic and Catalytic Applications. *J. Solid State Chem.* **2008**, *181*, 1552–1559.
(64) Toberer, E. S.; Rauwel, P.; Gariel, S.; Tafto, J.; Snyder, G. J. Composition and the Thermoelectric Performance of β-Zn_4Sb_3. *J. Mater. Chem.* **2010**, *20*, 9877–9885.
(65) Xiong, D.-B.; Okamoto, N. L.; Inui, H. Enhanced Thermoelectric Figure of Merit in p-Type Ag-Doped ZnSb Nanostructured with Ag_3Sb. *Scripta Mater.* **2013**, *69*, 397–400.
(66) Heremans, J. P.; Dresselhaus, M. S.; Bell, L. E.; Morelli, D. T. When Thermoelectrics Reached the Nanoscale. *Nat. Nanotech.* **2013**, *8*, 471–473.
(67) Dresselhaus, M. S.; Chen, G.; Tang, M. Y.; Yang, R. G.; Lee, H.; Wang, D. Z.; Ren, Z. F.; Fleurial, J.-P.; Gogna, P. New Directions for Low-Dimensional Thermoelectric Materials. *Adv. Mater.* **2007**, *19*, 1043–1053.
(68) Ibanez, M.; Luo, Z.; Genc, A.; Piveteau, L.; Ortega, S.; Cadavid, D.; Dobrozhan, O.; Liu, Y.; Nachtegaal, M.; Zebarjadi, M.; Arbiol, J.; Kovalenko, M. V.; Cabot, A. High-Performance Thermoelectric Nanocomposites from Nanocrystal Building Blocks. *Nat. Commun.* **2016**, *7*, 10766.
(69) Blichfeld, A. B.; Iversen, B. B. Fast Direct Synthesis and Compaction of Phase Pure Thermoelectric ZnSb. *J. Mater. Chem. C.* **2015**, *3*, 10543–10553.
(70) Clark, S. J.; Segall, M. D.; Pickard, C. J.; Hasnip, P. J.; Probert, M. J.; Refson, K.; Payne, M. C. First Principles Methods Using CASTEP. *Z. Kristallogr.* **2005**, *220*, 567–570.
(71) Rosales, B. A.; White, M. A.; Vela, J. Solution-Grown Sodium Bismuth Dichalcogenides: Toward Earth-Abundant, Biocompatible Semiconductors. *J. Am. Chem. Soc.* **2018**, *140*, 3736–3742.
(72) Chupas, P. J.; Chapman, K.W.; Kurtz, C.; Hanson, J.C.; Lee, P.L.; Grey, C. P. A Versatile Sample-Environment Cell for Non-Ambient X-ray Scattering Experiments. *J. Appl. Cryst.* **2008**, *41*, 822–824.
(73) Harris, R. K.; Becker, E. D.; De Menezes, S. M. C.; Goodfellow, R.; Granger, P. NMR Nomenclature. Nuclear Spin Properties and Conventions for Chemical Shifts (IUPAC Recommendations 2001). *Pure Appl Chem* **2001**, *73*, 1795–1818.
(74) Oas, T. G.; Griffin, R. G.; Levitt, M. H. Rotary Resonance Recoupling of Dipolar Interactions in Solid-State Nuclear Magnetic Resonance Spectroscopy. *J. Chem. Phys.* **1988**, 89 (2), 692–695.
(75) Schnell, I. Dipolar Recoupling in Fast-MAS Solid-State NMR Spectroscopy. *Prog. Nucl. Magn. Reson. Spectrosc.* **2004**, *45*, 145–207.
(76) Venkatesh, A.; Hanrahan, M. P.; Rossini, A. J. Proton Detection of MAS Solid-State NMR Spectra of Half-Integer Quadrupolar Nuclei. *Solid State Nucl. Magn. Reson.* **2017**, *84*, 171–181.
(77) Hung, I.; Schurko, R.W. Solid-State ^{91}Zr NMR of Bis(cyclopentadienyl)dichlorozirconium(IV). *J. Phys. Chem. B* **2004**, *108*, 9060–9069.
(78) Perras, F. A.; Widdifield, C. M.; Bryce, D. L. QUEST – QUadrupolar Exact SofTware: A Fast Graphical Program for the Exact Simulation of NMR and NQR Spectra for Quadrupolar Nuclei. *Solid State Nucl. Magn. Reson.* **2012**, *45–46*, 36–44.
(79) Faucher, A.; Terskikh, V. V.; Wasylishen, R. E. Feasibility of Arsenic and Antimony NMR Spectroscopy in Solids: An Investigation of Some Group 15 Compounds. *Solid State Nucl. Magn. Reson.* **2014**, *61–62*, 54–61.
(80) Perdew, J. P.; Burke, K.; Ernzerhof, M. Generalized Gradient Approximation Made Simple. *Phys. Rev. Lett.* **1996**, *77*, 3865–3868.
(81) Tkatchenko, A.; Scheffler, M. Accurate Molecular van der Waals Interactions from Ground-State Electron Density and Free-Atom Reference Data. *Phys. Rev. Lett.* **2009**, *102*, 073005.

(82) Yates, J. R.; Pickard, C. J.; Mauri, F. Calculation of NMR Chemical Shifts for Extended Systems Using Ultrasoft Pseudopotentials. *Phys. Rev. B: Condens. Matter Mater. Phys.* **2007**, *76*, 024401.

(83) Pickard, C. J.; Mauri, F. All-Electron Magnetic Response with Pseudopotentials: NMR Chemical Shifts. *Phys. Rev. B: Condens. Matter Mater. Phys.* **2001**, *63*, 245101.

(84) Kresse, G. From Ultrasoft Pseudopotentials to the Projector Augmented-Wave Method. *Phys. Rev. B* **1999**, *59*, 1758–1775.

(85) Blöchl, P. E. Projector Augmented-Wave Method. *Phys. Rev. B* **1994**, *50*, 17953–17979.

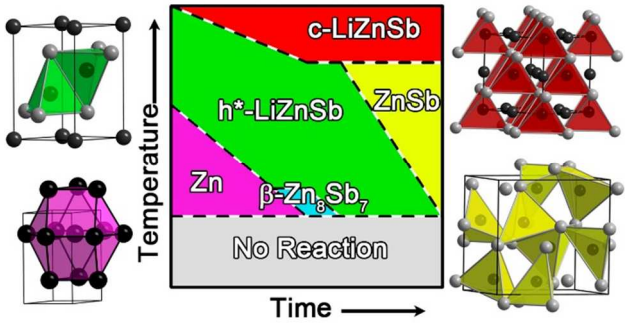

Insert Table of Contents artwork here